Wind Tunnel Verification of Velocity Control in Wing Coordinate System Using Acceleration-Based Disturbance Observer for Tilt-Wing eVTOL

Takuma Katagiri[*a] Student Member, Kentaro Yokota[**] Non-member

Kota Fujimoto[*] Student Member, Sakahisa Nagai[*] Member

Hiroshi Fujimoto[*] Senior Member

Recently, the development of electric vertical take-off and landing (eVTOL) has attracted much attention owing to their potential applications in various scenarios of human society, such as advanced transportation, surveillance, and inspections in hazardous environments. Among various eVTOL designs, the tilt-wing configuration stands out for its advantages, including reduced wing drag during ascent and effective utilization of propeller slipstream during transition phases. In this study, we propose a novel velocity control system designed in the wing coordinate system, employing an acceleration-based disturbance observer for tilt-wing eVTOLs. This method achieves enhanced disturbance rejection and decoupled control. The proposed approach was validated through computer simulations and hardware-in-the-loop simulations conducted in a wind tunnel.

Keywords: tilt-wing, eVTOL, velocity control, disturbance observer

1. Introduction

1.1 Background of eVTOL A vertical take-off and landing (VTOL) has been developed since the 1900s because of its advantage of not requiring a runway for take-off and landing. In recent years, an electric VTOL (eVTOL) has attracted great attention because of technological developments such as high-performance batteries, electric propulsion technology, and automatic driving technology[2][3] to provide a new means of transportation[4] or to play roles in monitoring and surveillance in dangerous places. To realize an eVTOL system, electric propulsion technology is especially a key technology. It has the advantages of fast torque response and quick thrust control[5], which also provides accurate torque estimation and enables us to power regeneration[6]. Taking advantage of these capabilities, we have been studying new control methods such as airspeed estimation using motor current measurements[7], and fast and efficient thrust control of variable-pitch-propeller[8].

There are two types of eVTOLs: fixed-wing type and rotary-wing type. This paper focuses on the fixed-wing type eVTOL which can fly longer distances than the rotary-wing type. Among fixed-wing type eVTOLs, the tilt-wing type is superior in terms of a smaller drag force on the wings than the tilt-rotor type during ascent because the wings face upward.
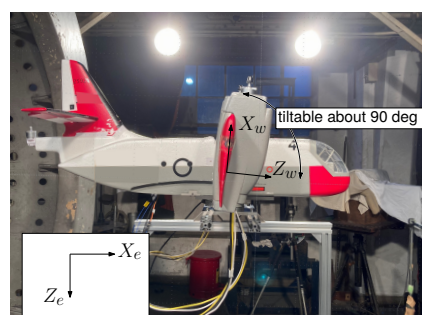
Fig. 1: The tilt-wing eVTOL used in wind tunnel experiment with earth-fixed coordinate system and wing coordinate system.

In addition, it can use the propeller slipstream during transition. In this paper, we focus on tilt-wing eVTOL such as Fig. 1 because of these advantages.

1.2 Literature review on tilt-wing eVTOL The tilt-wing eVTOLs are prone to become unstable during transitions because the aerodynamic characteristics are significantly changed by tilting the wing angle. To cope with this problem, many studies have been conducted on attitude control[9] and velocity control[10]–[12].

In Ref. (9), a controller was designed for a tandem tilt-wing aircraft to stabilize the flight for both longitudinal and lateral-directional motions. It shows a complete transition from hover to cruise and vice versa under the control of a pilot; however, velocity control is not considered. In Ref. (10), velocity control of a tilt-wing aircraft is performed in a wide range of velocity commands using a feedforward controller obtained from wind tunnel testing. However, in the experimental results, there are steady-state errors in the velocity response. In Ref. (11), cruise control is validated in experiments for

Table 1: Parameter definitions.

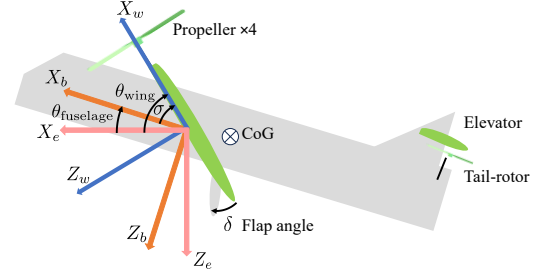| Parameter	Definition	Unit
ρ	air density	kg/m^3
D_{p}	propeller diameter	m
n_{p}	the number of propellers in the main wing	m
S_a	wing area	m^2
S_s	wing area in slipstream	m^2
m	mass of aircraft	kg
I_b	inertia of aircraft around Y_b axis	kg m^2
ω	propeller angular velocity	rad/s
δ	flap angle	deg
σ	tilt angle	deg
α	angle of attack	deg
$\theta_{\mathrm{fuselage}}$	pitch angle of aircraft body	rad
θ_{wing}	angle between main wing and ground	rad
$r = [X, Z]^\top$	position of aircraft	m
$V = [V_x, V_z]^\top$	velocity of aircraft	m/s
$a = [a_x, a_z]^\top$	acceleration of aircraft	m/s^2
v	airspeed vector	m/s
F	thrust produced by a propeller	N
F_{th}	force vector produced by the propeller thrust	N
F_{aero}	aerodynamic force vector	N
F_{w}	aerodynamic force vector produced by the wing	N
F_{b}	aerodynamic force vector produced by the body	N
F_{g}	gravity vector	N
F_{tail}	force created by the elevator and the tail rotor	N
M_{th}	moment produced by the propeller thrust around Y_b axis	N m
M_{w}	moment produced by the wing around Y_b axis	N m
M_{tail}	moment produced by the elevator and the tail rotor	N m
$(\cdot)_e$	variables in the earth-fixed coordinates	–
$(\cdot)_w$	variables in the wing coordinates	–
$(\cdot)_b$	variables in the body coordinates	–

Fig. 2: Model of aircraft. $[X_e, Z_e]$ are the earth-fixed coordinates. $[X_b, Z_b]$ are the body coordinates. $[X_w, Z_w]$ are the wing coordinates.

paper focuses on the sagittal plane motion.

This paper is organized as follows: Section 2 describes the simulation model, Section 3 describes the proposed control system and Section 4 describes the simulation results. Section 5 describes the HILS results, and finally, Section 6 describes the conclusion.

2. Modeling

2.1 Equation of motion Fig. 2 shows the model of the tilt-wing eVTOL used in this paper. It has a main wing whose tilt angle can be changed, an elevator, and a tail rotor. The main wing has four propellers and two flaps. By controlling the propeller and flap, the forces acting on the aircraft can be changed. The dynamic motion of the aircraft can be expressed by the following equations:

$$m \frac{\mathrm{d}^2}{\mathrm{d}t^2} \begin{bmatrix} X_e \\ Z_e \end{bmatrix} = F_{\mathrm{th}}(\omega) + F_{\mathrm{aero}}(\omega, \delta) + F_{\mathrm{g}} + F_{\mathrm{tail}}, \quad (1)$$

$$I_b \frac{\mathrm{d}^2}{\mathrm{d}t^2} \theta_{\mathrm{fuselage}} = M_{\mathrm{th}}(\omega) + M_{\mathrm{aero}}(\omega, \delta) + M_{\mathrm{tail}}. \cdots (2)$$

The variables' definition is listed in Table 1. In this paper, it is assumed that the pitch angle of the aircraft is always controlled by an elevator and a tail-rotor to 0 deg, i.e., $\theta_{\mathrm{fuselage}} = 0$ and the created force by them is small enough. Therefore, only the translational motion is considered. Under this assumption, Eq. (1) can be rewritten as the below equation:

$$m \frac{\mathrm{d}^2}{\mathrm{d}t^2} \begin{bmatrix} X_e \\ Z_e \end{bmatrix} = F_{\mathrm{th}}(\omega) + F_{\mathrm{aero}}(\omega, \delta) + F_{\mathrm{g}}. \cdots\cdots (3)$$

$F_{\mathrm{aero}}(\omega, \delta)$ is aerodynamic force, and it is a sum of forces produced by the wing $F_{\mathrm{w}}(\omega, \delta)$ and forces produced by the body F_b.

2.2 Propeller model The thrust generated by the propeller can be calculated using the thrust coefficient $C_F(J)$ as follows:

$$F(J, \omega) = C_F(J) \rho \frac{\omega^2}{4\pi^2} D_{\mathrm{p}}^4, \cdots\cdots\cdots\cdots\cdots (4)$$

J is the advance ratio defined as $J = \frac{2\pi v_\perp}{\omega D_{\mathrm{p}}}$. $v_\perp$ is the propeller perpendicular component of the airspeed vector, which is calculated as $v_\perp = v \cos\alpha$, where α is the angle of attack. $C_F(J)$ are the function of J, and they are fitted from the data provided by Ref. (18) as shown in Fig. 3(a). Using Eq. (4), $F_{\mathrm{th}}(\omega)$ is calculated as

$$F_{\mathrm{th}}(\omega) = \begin{bmatrix} n_{\mathrm{p}} F(J, \omega) \cos\theta_{\mathrm{wing}} \\ -n_{\mathrm{p}} F(J, \omega) \sin\theta_{\mathrm{wing}} \end{bmatrix}, \cdots\cdots\cdots\cdots (5)$$

the transition state. It uses a feedforward controller and a feedback controller to track velocity commands and shows good performance in vertical velocity tracking. However, this feedback method has two disadvantages. First, the wind disturbance rejection performance is not discussed. Second, there is a modeling error caused by linearization. Ref. (12) is a paper on velocity control using Nonlinear Model Predictive Control (NMPC) written by the same group with Ref. (11). It provides good tracking performance in both vertical and horizontal velocity reference. However, the sampling time of NMPC is 0.1 s, and it is slower than motor response. To improve disturbance rejection performance, an inner layer controller should be sophisticated.

1.3 Contributions of this paper To solve the above problems, we propose a novel velocity feedback control using a disturbance observer (DOB). DOB was first proposed in the 1980s, and its effectiveness and ease of application have been verified by numerous research in recent years[13][14]. Some research applied DOB to a quadcopter[15]–[17], however, to the best of the authors' knowledge, no one applied it to velocity control of a tilt-wing eVTOL.

In this paper, the proposed DOB is applied to the tilt-wing eVTOL to introduce the wing coordinate system. It enables us to construct a velocity controller easily, and it has strength in disturbance rejection and decoupling control of thrust force and flap force. This idea is an expansion of our previous research on aerodynamic force control system using DOB[7]. We expand it to velocity control for the full body system using acceleration measurement. The effectiveness of our proposed method is validated by computer simulations and hardware-in-the-loop simulations (HILS) using a wind tunnel. This
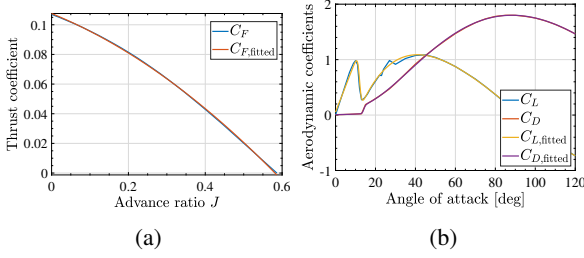
Fig. 3: Coefficients used in the simulation. (a) Thrust coefficient[18]. (b) Lift and drag coefficients of NACA0012 airfoil[19].
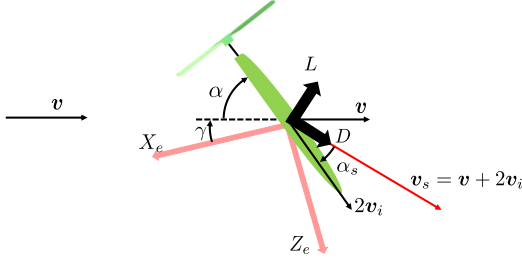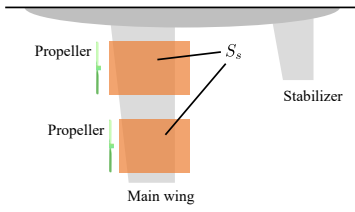

Fig. 4: Diagram of propeller-wing model.

Fig. 5: Wing area in slip stream S_s.

where n_p is the number of propellers in the main wing, and θ_{wing} is an angle between the main wing and the ground.

2.3 Propeller-wing model A schematic diagram of the propeller-wing model is shown in Fig. 4. In the figure, γ is an angle between ground and airspeed vector v. From momentum theory, the induced velocity near the propeller v_i is expressed as

$$v_i = \frac{1}{2}\left(-v_\perp + \sqrt{v_\perp^2 + \frac{2F}{\rho A}}\right) \cdots\cdots\cdots\cdots\cdots\cdots (6)$$

where A is the area of a propeller as a disk. Using this expression, the propeller-derived wind speed can be expressed as $2v_i$ based on the momentum theory. By combining with the airspeed v, wind velocity acting on the wing v_s and α_s in Fig. 4 can be expressed as

$$v_s = |v_s| = \sqrt{(v\sin\alpha)^2 + (2v_i + v\cos\alpha)^2}, \cdots\cdots (7)$$

$$\alpha_s = \arctan\left(\frac{v\sin\alpha}{2v_i + v\cos\alpha}\right) \cdots\cdots\cdots\cdots\cdots\cdots (8)$$

where α is angle of attack expressed as $\alpha = \theta_{wing} - \gamma$.

2.4 Wing model The forces produced by wing $F_w(\omega, \delta)$ is a sum of the forces produced by the wing with or without the propeller slipstream, i.e., $F_w(\omega, \delta) = F_{w_{s-a}}(\delta) + F_{w_s}(\omega, \delta)$. Fig. 5 shows a definition of the area in the slipstream S_s. Lift and drag forces produced by the airfoil where is out of the propeller slipstream are calculated as
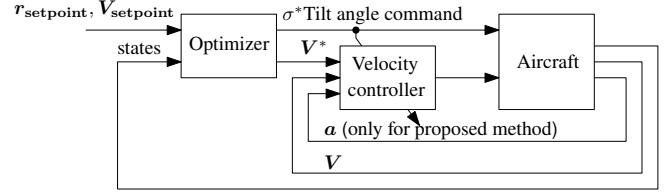

Fig. 6: Translational motion control system of aircraft. Velocity controller is the target of this study.

$$L_{a-s} = \frac{1}{2}C_L(\alpha, \delta)\rho(S_a - S_s)v^2, \cdots\cdots\cdots\cdots (9)$$

$$D_{a-s} = \frac{1}{2}C_D(\alpha, \delta)\rho(S_a - S_s)v^2 \cdots\cdots\cdots\cdots (10)$$

where S_a is the area of all airfoil and S_s is the area of airfoil in the propeller slipstream. C_L and C_D called lift coefficients and drag coefficients. In this paper, the lift and drag coefficient is affected by flap angle δ, and modeled as[20]

$$C_L(\alpha, \delta) = C_L(\alpha) + C_{L0}\delta, \cdots\cdots\cdots\cdots\cdots (11)$$

$$C_D(\alpha, \delta) = C_D(\alpha) + C_{D0}\delta^2. \cdots\cdots\cdots\cdots\cdots (12)$$

Experimental data for NACA0012 airfoil at Reynolds number 3.6×10^5 reported in Ref. (19) is used in computer simulations; whose characteristics are shown in Fig. 3(b).

From Eq. (9) and Eq. (10), $F_{w_{s-a}}$ is calculated as

$$F_{w_{a-s}}(\delta) = \begin{bmatrix} -L_{a-s}\sin\gamma - D_{a-s}\cos\gamma \\ -L_{a-s}\cos\gamma + D_{a-s}\sin\gamma \end{bmatrix} \cdots\cdots\cdots (13)$$

Using the propeller slipstream model shown in Subsection 2.3, the lift and drag forces produced by the airfoil where is in the propeller slipstream are calculated as

$$L_s = \frac{1}{2}C_L(\alpha_s, \delta)\rho S_s v_s^2, \cdots\cdots\cdots\cdots\cdots\cdots (14)$$

$$D_s = \frac{1}{2}C_D(\alpha_s, \delta)\rho S_s v_s^2. \cdots\cdots\cdots\cdots\cdots\cdots (15)$$

Using Eq. (14) and (15), F_{w_s} is calculated as

$$F_{w_s}(\omega, \delta) = \begin{bmatrix} -L_s\sin(\theta_{wing} - \alpha_s) - D_s\cos(\theta_{wing} - \alpha_s) \\ -L_s\cos(\theta_{wing} - \alpha_s) + D_s\sin(\theta_{wing} - \alpha_s) \end{bmatrix}. \tag{16}$$

To summarize the above, forces produced by the wing $F_w(\omega, \delta)$ is calculated by the sum of Eq. (13) and Eq. (16).

2.5 Aerodynamic force of the body As the same with the drag force of the wing model, the body drag force is modeled as proportional to the square of the wind velocity,

$$F_b = \begin{bmatrix} -\frac{1}{2}\rho v_{x_e}|v_{x_e}|S_{body_x} \\ -\frac{1}{2}\rho v_{z_e}|v_{z_e}|S_{body_z} \end{bmatrix}, \cdots\cdots\cdots\cdots\cdots\cdots (17)$$

where S_{body_x} and S_{body_z} are the coefficient that characterizes the body drag force.

3. Proposed velocity control system

3.1 Translational motion control system structure The translational motion control system of aircraft is shown in Fig. 6. In the figure, the optimizer represents the outer layer controller, and it has a role in creating the feasible trajectory of tilt angle and velocity against wind conditions when given the

position and velocity set point. The inner layer controller: the velocity controller, has a role in tracking the two-dimensional trajectory using the propeller thrust and flap deflection. We use a propeller and flap because their response is faster than the tilt angle response. This paper focuses on the velocity controller.

3.2 Conventional method The conventional velocity controller is shown in Fig. 7[11]. In Ref. (11), the control allocation based on the following optimization problem is applied:

$$\min_{\boldsymbol{u}^*} \left(\boldsymbol{H}\boldsymbol{u}^* - \boldsymbol{a}_e^*\right)^\top \boldsymbol{W} \left(\boldsymbol{H}\boldsymbol{u}^* - \boldsymbol{a}_e^*\right) + \left(\boldsymbol{u}^*\right)^\top \boldsymbol{K}\boldsymbol{u}^*$$
$$\text{s.t. } \boldsymbol{u}^* \in [\boldsymbol{u}_{\min} \ \boldsymbol{u}_{\max}] \cdots\cdots\cdots\cdots\cdots\cdots\cdots (18)$$

$\boldsymbol{W}$ is a weighting matrix and $\boldsymbol{K}$ is a regularization matrix. $\boldsymbol{u}^*$ and $\boldsymbol{H}$ are as follows:

$$\boldsymbol{u}^* = \begin{bmatrix} \Delta\theta_{\text{fuselage}} \\ \Delta\omega \end{bmatrix}, \ \boldsymbol{H} = \begin{bmatrix} \frac{\partial a_{x_e}}{\partial \theta_{\text{fuselage}}} & \frac{\partial a_{x_e}}{\partial \omega} \\ \frac{\partial a_{z_e}}{\partial \theta_{\text{fuselage}}} & \frac{\partial a_{z_e}}{\partial \omega} \end{bmatrix} \cdots (19)$$

To compare the conventional method and the proposed method, the pitch angle input is converted to the flap angle. In addition, by setting the regularization matrix $\boldsymbol{K}$ at $\boldsymbol{0}$ and ignoring the constraints of the actuator as a simple implementation, the following equation is used for control allocation:

$$\begin{bmatrix} \Delta\omega^* \\ \Delta\delta^* \end{bmatrix} = \boldsymbol{A}_{\text{n}}^{-1}(v_{x_b}, \theta_{\text{wing}}) \begin{bmatrix} a_{x_w}^* \\ a_{z_w}^* \end{bmatrix}, \ \cdots\cdots\cdots\cdots (20)$$

where $\boldsymbol{A}_{\text{n}}$ is a nominal value of $\boldsymbol{A}$, and $\boldsymbol{A}$ is expressed as follows:

$$\boldsymbol{A} = \begin{bmatrix} \frac{\partial a_{x_w}}{\partial \omega} & \frac{\partial a_{x_w}}{\partial \delta} \\ \frac{\partial a_{z_w}}{\partial \omega} & \frac{\partial a_{z_w}}{\partial \delta} \end{bmatrix} \cdots\cdots\cdots\cdots\cdots\cdots (21)$$

$\boldsymbol{A}_{\text{n}}$ is 2×2 matrix and which is scheduled at airspeed in the X_b direction v_{x_b}, and wing angle θ_{wing}. $\Delta\omega$ and $\Delta\delta$ are deviations from operating point ω_0, δ_0. The acceleration $\boldsymbol{a}$ is equal to $\boldsymbol{0}$ at the operating point. In the figure, $\boldsymbol{R}$ is a rotational matrix that converts from the earth-fixed coordinate system to the wing coordinate system, which is defined as:

$$\boldsymbol{R}(\theta_{\text{wing}}) = \begin{bmatrix} \cos\theta_{\text{wing}} & -\sin\theta_{\text{wing}} \\ \sin\theta_{\text{wing}} & \cos\theta_{\text{wing}} \end{bmatrix} \cdots\cdots\cdots\cdots (22)$$

3.3 Proposed velocity control system We propose the wing coordinate velocity control system with acceleration-based DOB whose block diagram is shown in Fig. 8. From Eq. (5), Eq. (13) and Eq. (16), propeller rotation speed ω and flap angle δ affect forces in both the X_e and Z_e directions, so it is not possible to generate the forces acting on only one axis with a single actuator. Moreover, the magnitude of this interference depends on the wing angle. By introducing the wing coordinate system, the propeller can control the force parallel to the wing, and the flap can control the force perpendicular to the wing, but they are not completely independent. There is interference, such as an increase in propeller thrust increasing lift, or an increase in flap angle increasing drag. This is resolved in the proposed method by using the DOB with acceleration obtained from an inertial measurement unit (IMU). The plant system can be viewed as a SISO system thanks to the decoupling part, so the control system can be

designed easily. In addition, it is possible to compensate for high-frequency disturbances and modeling errors by the proposed DOB system.

In the figure, each saturation block limits the output of the block to $[\omega_{\min} - \omega_0, \omega_{\max} - \omega_0]$ and $[\delta_{\min} - \delta_0, \delta_{\max} - \delta_0]$, respectively. $\omega_{\min}$, $\omega_{\max}$, $\delta_{\min}$, and $\delta_{\max}$ are the limits of the actuators.

Eq. (3) can be rewritten in wing coordinates as follows:

$$m\boldsymbol{a}_w = \boldsymbol{R}(\theta_{\text{wing}}) \left\{ \boldsymbol{F}_{\text{th}}(\omega) + \boldsymbol{F}_{\text{aero}}(\omega, \delta) + \boldsymbol{F}_{\text{g}} \right\} \cdots (23)$$

To derive the equation, $\dot{\theta}_{\text{wing}} = 0$ is assumed. The equation can be linearized around the operating point as follows:

$$m\boldsymbol{a}_w = \boldsymbol{R}(\theta_{\text{wing}}) \left\{ \boldsymbol{F}_{\text{th}}(\omega_0) + \boldsymbol{F}_{\text{aero}}(\omega_0, \delta_0) + \boldsymbol{F}_{\text{g}} \right\} + m\boldsymbol{A} \begin{bmatrix} \Delta\omega \\ \Delta\delta \end{bmatrix} .(24)$$

Here, ω_0 and δ_0 represent the nominal values of the actuator output which balance the forces acting on the aircraft, however, forces do not always balance even when ω_0 and δ_0 are applied due to modeling errors and vertical wind conditions. Let us define $\tilde{\boldsymbol{d}}_{\text{op}}$ as

$$\tilde{\boldsymbol{d}}_{\text{op}} = \boldsymbol{F}_{\text{th}}(\omega_0) + \boldsymbol{F}_{\text{aero}}(\omega_0, \delta_0) + \boldsymbol{F}_{\text{g}}, \cdots\cdots\cdots\cdots (25)$$

which can be said as the modeling error of the operating point. If there is no modeling error for ω_0 and δ_0, $\boldsymbol{F}_{\text{th}}(\omega_0) + \boldsymbol{F}_{\text{aero}}(\omega_0, \delta_0)$ is canceled with $\boldsymbol{F}_{\text{g}}$. However, it is not realized; that is $\tilde{\boldsymbol{d}}_{\text{op}} \neq \boldsymbol{0}$. Using $\tilde{\boldsymbol{d}}_{\text{op}}$, Eq. (24) can be rewritten as

$$\boldsymbol{a}_w = \frac{1}{m}\boldsymbol{R}(\theta_{\text{wing}})\tilde{\boldsymbol{d}}_{\text{op}} + \boldsymbol{A} \begin{bmatrix} \Delta\omega \\ \Delta\delta \end{bmatrix} \cdots\cdots\cdots\cdots (26)$$

Using this equation, the block diagram of the linearized plant and DOB is shown in Fig. 9. In the figure,

$$\boldsymbol{A}_{\text{d,n}}(v_{x_b}, \theta_{\text{wing}}) = \text{diag}\{A_{11,\text{n}}(v_{x_b}, \theta_{\text{wing}}), A_{22,\text{n}}(v_{x_b}, \theta_{\text{wing}})\}, (27)$$

$$\boldsymbol{G}_{\text{n}}(s) = \text{diag}\left\{\frac{1}{\tau_{\text{th}}s + 1}, \frac{1}{\tau_{\delta}s + 1}\right\}, \cdots\cdots\cdots\cdots (28)$$

$$\boldsymbol{Q}(s) = \text{diag}\left\{\frac{\omega_{\text{DOB}}}{s + \omega_{\text{DOB}}}, \frac{\omega_{\text{DOB}}}{s + \omega_{\text{DOB}}}\right\}, \cdots\cdots\cdots (29)$$

$$\boldsymbol{d} = [d_{\text{th}}, d_\delta]^\top, \cdots\cdots\cdots\cdots\cdots\cdots\cdots\cdots\cdots (30)$$

and $\boldsymbol{G}(s)$ is a diagonal matrix whose elements are the true dynamics of each actuator. τ_{th} and τ_δ are the nominal time constant of propeller speed control and flap angle control. ω_{DOB} is a cutoff frequency of the DOB. $A_{11,\text{n}}$ and $A_{22,\text{n}}$ are the diagonal elements of matrix $\boldsymbol{A}_{\text{n}}$, and expressed as follows:

$$A_{11,\text{n}}(v_{x_b}, \theta_{\text{wing}}) = \left. \frac{\partial a_{x_w}}{\partial \omega} \right|_{\omega=\omega_0(v_{x_b}, \theta_{\text{wing}}), \delta=\delta_0(v_{x_b}, \theta_{\text{wing}})}, (31)$$

$$A_{22,\text{n}}(v_{x_b}, \theta_{\text{wing}}) = \left. \frac{\partial a_{z_w}}{\partial \delta} \right|_{\omega=\omega_0(v_{x_b}, \theta_{\text{wing}}), \delta=\delta_0(v_{x_b}, \theta_{\text{wing}})}. (32)$$

It means that $A_{11,\text{n}}$, $A_{22,\text{n}}$, ω_0, and δ_0 are scheduled at wind speed parallel to the body v_{x_b} and wing angle θ_{wing}, and we assume that v_{x_b} is obtained from a pitot tube. In this paper, the situation where v_{x_b} and θ_{wing} is constant is considered. Disturbance vector $\boldsymbol{d}$ is described as follows:

$$\boldsymbol{d} = \left(\boldsymbol{G}_{\text{n}}(s)^{-1}\boldsymbol{A}_{\text{d,n}}^{-1} - \boldsymbol{G}(s)^{-1}\boldsymbol{A}^{-1}\right)\boldsymbol{a}_w + \boldsymbol{d}_{\text{op}}. \cdots\cdots (33)$$
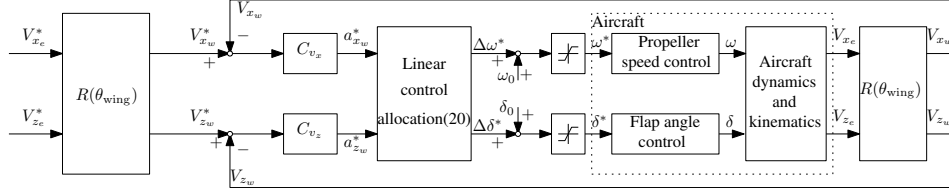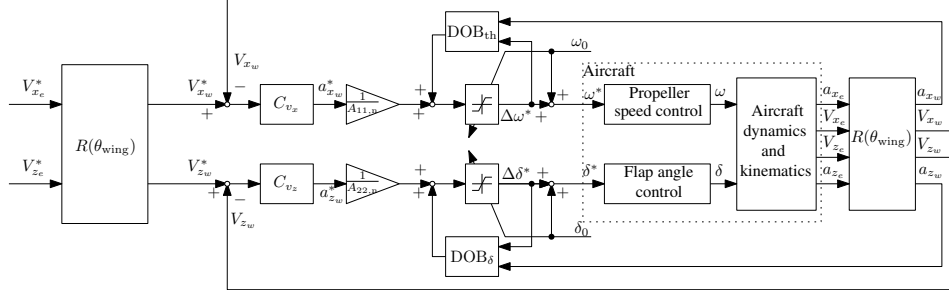
Fig. 7: Conventional velocity control system.

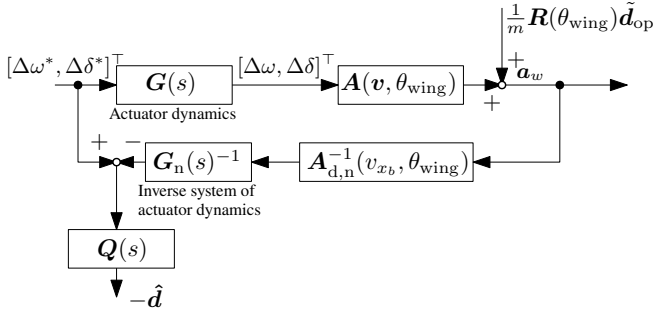

Fig. 8: Proposed wing coordinate velocity control system.

Fig. 9: Block diagram of linearized plant and DOB.

Table 2: Aircraft parameter.

Symbol	Description	Value
m	mass of aircraft	2.0 kg
–	wingspan	1.2 m
S_a	wing area	0.30 m^2
S_s	wing area in slipstream	0.25 m^2
D_p	propeller diameter	0.254 m

Table 3: Controller settings in the simulation.

Symbol	Description	Value
–	pole of velocity controller (prop. and conv.)	1.5 rad/s
τ_th	nominal time constant of propeller angular velocity controller	0.1 s
τ_δ	nominal time constant of flap angle controller	0.063 s
ω_DOB	cutoff frequency of DOB	5 rad/s

(a)

(b)

(c)

Fig. 10: The simulation result for performance validation of disturbance rejection. (a) V_{x_e}. (b) V_{z_e}. (c) Wind disturbance.

The first term contains the coupling disturbance and the modeling error of $A_\mathrm{d,n}$ and the actuator dynamics, and the second term contains the disturbance equivalent to the modeling error of the operating point, i.e., $d_\mathrm{op} = G^{-1}(s)A^{-1}\frac{1}{m}R(\theta_\mathrm{wing})\tilde{d}_\mathrm{op}$. The DOB estimates the disturbance d and suppresses it. Since the control system is configured in the wing coordinates, the pitch angle variation has no significant effect on matrix A. However, pitch angle variation changes the drag force of the body. It means that the value of d_op changes, but it does not matter because pitch angle variation is usually under the cut-off frequency of the DOB, and the disturbance is suppressed by the DOB.

4. Simulation

We show two simulations to evaluate disturbance rejection performance and decoupling control performance. The aircraft parameters are shown in Table 2. The controller settings are shown in Table 3. An I-P controller is selected as each velocity controller C_v for fair comparison and is designed by pole placement for the nominal plant $\frac{1}{s}$. The cutoff frequency of the DOB is tuned by trial and error. Various values of ω and δ are input to the aircraft simulation model, and acceleration a is obtained. These values are used to obtain matrix $A_\mathrm{d,n}$ and A_n by linearly approximating the relationships from propeller rotation speed ω and flap angle δ to acceleration a_{x_w} and a_{x_w}.
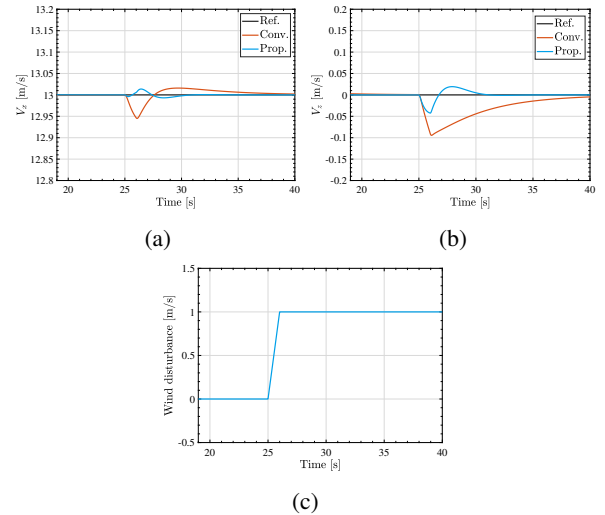
4.1 Disturbance rejection We assume that a situa-

tion where the ramp headwind disturbance shown in Fig. 10(c) is applied during forward flight at a tilt angle of 3 deg and a velocity command of 11 m/s. This wind generates a disturbance force magnitude of -0.90 N and -2.6 N in the X_e direction
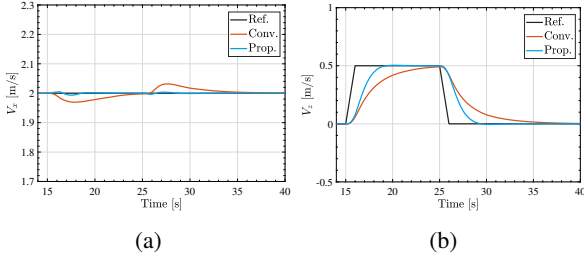
(a)   (b)

Fig. 11: The simulation result for performance validation of decoupling control. (a) V_{x_e}. (b) V_{z_e}.
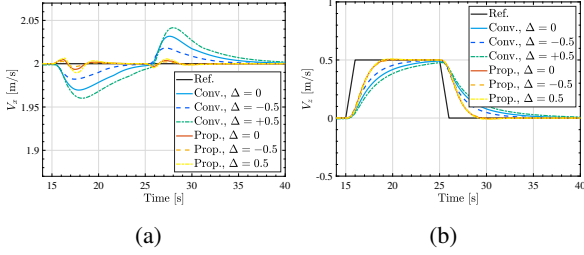

(a)   (b)

Fig. 12: The simulation result for performance validation of decoupling control when modeling errors exist. (a) V_{x_e}. (b) V_{z_e}.

and the Z_e direction. Fig. 10 shows the simulation results. It shows that the proposed velocity control system can compensate for the wind disturbance faster than the conventional method.

4.2 Decoupling control In this subsection, the situation where we only control Z_e the direction velocity while the aircraft has the constant speed in X_e the direction is considered. If perpendicular force and parallel force to the wing can be controlled independently, velocity measurement in X_e the direction should be maintained as a constant value. In this simulation, the tilt angle is set at 50 deg, and the velocity command in the X_e direction $V_{x_e}^*$ is set at 2 m/s. Fig. 11 shows the simulation results. Fig. 11(a) shows that the proposed method has less error in V_{x_e}, meaning that the proposed method has better decoupling performance than the conventional method. Fig. 11(b) shows the tracking performance in the Z_e direction, and we tried to keep tracking performance in the Z_e direction the same by designing the same velocity controller C_v, however slightly differs because of nonlinearity and coupling terms of the plant.

Generally modeling errors could affect the control performance. We conducted the simulation to assess the effect of modeling error. Modeling error Δ is defined as follows:

$$\begin{cases} A_{d,n} = A_d + \Delta A_d & \text{(In proposed method.)} \\ A_n = A + \Delta A & \text{(In conventional method.)} \end{cases} \cdots (34)$$

A_d is a diagonal term of matrix A in Eq. (21), and it is obtained from the simulation model. A simulation is conducted under the same situation as the decoupling control simulation but with a modeling error of $\Delta = \pm 50\%$. Simulation results are shown in Fig. 12. It shows that when large modeling error exists, the proposed method can effectively suppress the disturbance caused by the modeling error and the velocity can be accurately controlled.
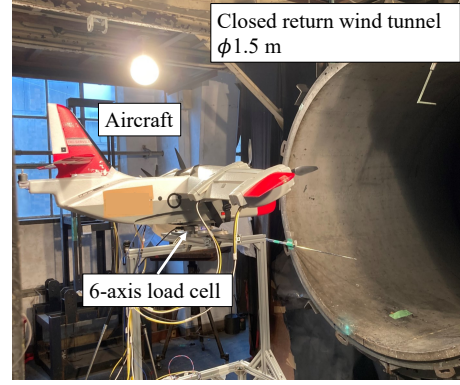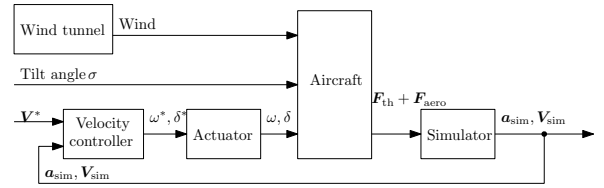

Fig. 13: Experimental setups.

Fig. 14: Block diagram of HILS.

Table 4: Controller settings in the HILS.

Symbol	Description	Value
−	pole of velocity controller (prop. and conv.)	1.5 rad/s
τ_{th}	nominal time constant of propeller angular velocity controller	0.1 s
τ_δ	nominal time constant of flap angle controller	0.063 s
ω_{DOB}	cutoff frequency of DOB	3 rad/s

5. Experiment

HILS is conducted to validate the proposed method in this section. The experimental setup is shown in Fig. 13. The wind tunnel has a closed return system, whose diameter is 1.5 m. Forces applied to the body are measured with a 6-axis load cell. The actuator command is generated by the controller outside the aircraft. An I-P controller is selected as each velocity controller C_v for fair comparison and is designed by pole placement for the nominal plant $\frac{1}{s}$. Sensorless PID feedback control is performed in the motor driver for the propeller.

The block diagram of HILS is shown in Fig. 14. In the simulator block, the calculation is conducted as follows:

$$a_{\text{sim}}(t) = \frac{1}{m} \left(F_{\text{th}} + F_{\text{aero}} + F_g \right), \cdots\cdots\cdots\cdots (35)$$

$$V_{\text{sim}}(t) = \int_0^t a_{\text{sim}}(\tau) d\tau. \cdots\cdots\cdots\cdots\cdots\cdots (36)$$

$F_{\text{th}} + F_{\text{aero}}$ is measured with a 6-axis load cell. F_g is a constant value added to load cell measurement because the offset including gravity is removed before measurement. In this experiment, the aircraft mass m is set at 1.5 kg because large mass leads to high loads to the motor during a long-duration experiment. The controller settings in the HILS are shown in Table 4.

5.1 Disturbance rejection The situation is the same as the disturbance rejection simulation in Subsection 4.1, however, some setting values are different. The tilt angle is set at 25 deg, and the velocity command in the X_e direction $V_{x_e}^*$
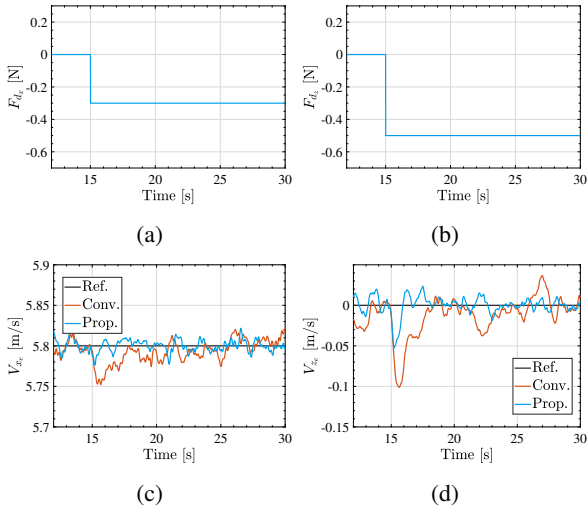
(a)

(b)

(c)

(d)

Fig. 15: The HILS result for performance validation of disturbance rejection. (a) Time series of software disturbance in the X_e direction (b)Time series of software disturbance in the Z_e direction. (c) V_{x_e}. (d) V_{z_e}.
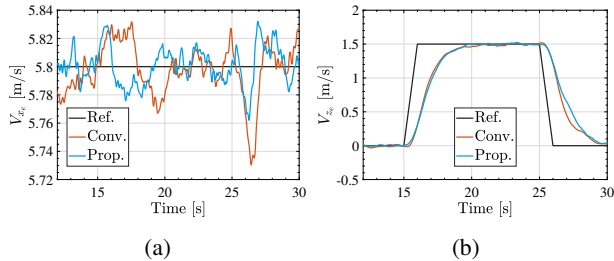

(a)

(b)

Fig. 16: The HILS result for performance validation of decoupling control. (a) V_{x_e}. (b) V_{z_e}.

is set at 5.8 m/s. To evaluate headwind disturbance rejection performance, a software step disturbance was applied in both the X_e and Z_e direction. The magnitude of software disturbance is shown in Fig. 15(a)(b). The ratio of the magnitudes in the X_e and Z_e directions was determined from the ratio of the lift and drag coefficients at the tilt angle of 25 deg, and the magnitudes were determined by trial and error so that differences in the velocity responses are visible. The HILS result is shown in Fig. 15(c)(d), and RMSE is shown in Fig. 17(a). Fig. 15(c)(d) shows that the proposed method reduced the maximum error and showed fast suppression of disturbances. Fig. 17(a) shows that proposed method reduced RMSE 67% in the X_e direction and 60% in the Z_e direction compare to conventional method. This means that the proposed method has better disturbance rejection performance than the conventional method.

5.2 Decoupling control   The situation is the same as the decoupling control simulation in Subsection 4.2, however, some setting values are different. The tilt angle is set at 25 deg, and the velocity command in the X_e direction $V_{x_e}^*$ is set at 5.8 m/s.

Experimental results to validate the decoupling control performance are shown in Fig. 16, and RMSE in the X_e direction of the experiments is shown in Fig. 17(b). Fig. 16(b) demonstrates the tracking performance in the Z_e direction. In this experiment, the response speeds of the conventional and pro-
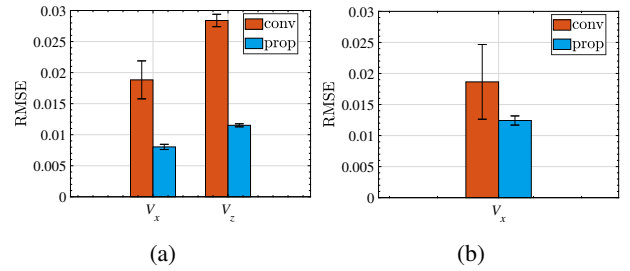

(a)

(b)

Fig. 17: RMSE of velocity in the HILS. Each experiment is conducted three times. The mean and standard deviation of RMSE are shown. (a) HILS for evaluating disturbance rejection performance. (b) HILS for evaluating decoupling control performance.

posed method are matched by pole placement. The reason why transient response of the V_{z_e} differs between conventional method and proposed method is the modeling error of matrix A due to the linear approximation in Eq. (21). In the HILS experiment, difference in transient response of V_{z_e} is smaller than simulation, and modeling error of matrix A is smaller in the HILS than our assumption. Fig. 16(a) and Fig. 17(b) show the tracking performance in the X_e direction, and it shows that the proposed method has less error in the X_e direction than the conventional method. Fig. 16(a) shows that the proposed method reduced the maximum error that comes from the coupling term. Fig. 17(b) shows that proposed method reduced RMSE 33% in the X_e direction compare to conventional method. That is, the proposed method has good decoupling control performance.

6. Conclusion

We proposed a velocity control system that has strength in easy tuning, disturbance rejection, and decoupling control for tilt-wing eVTOL. By introducing a wing coordinate system and using an acceleration-based disturbance observer, it is possible to consider the control system as two SISO systems. Computer simulation and HILS were conducted to assess the disturbance rejection and decoupling control performance. The results show that the proposed method has better performance than the conventional one in terms of disturbance rejection and decoupling control. In future works, an upper layer controller to obtain the optimized velocity reference is scrutinized, and the flight test including the proposed control system will be conducted.

References

(1) T. Katagiri, K. Yokota, K. Fujimoto, S. Nagai, and H. Fujimoto, "Basic study on velocity control in wing coordinate system using acceleration-based disturbance observer for tilt-wing eVTOL," in *10th IEEJ international workshop on Sensing, Actuation, Motion Control, and Optimization (SAMCON2024)*, (Kyoto, Japan), pp. 115–120, IEEJ, 2024.

(2) F. Hirahara, K. Uchida, and S. Hara, "Influences of aerodynamic parameter

7

IEEJ Trans. IA, Vol.144, No.1, 2024

uncertainties for UFSC based flight trajectory generation," *SICE Journal of Control, Measurement, and System Integration*, vol. 16, no. 1, pp. 363–372, 2023.

(3) R. Penicka and D. Scaramuzza, "Minimum-time quadrotor waypoint flight in cluttered environments," *IEEE Robotics and Automation Letters*, vol. 7, no. 2, pp. 5719–5726, 2022.

(4) L. A. Garrow, B. J. German, and C. E. Leonard, "Urban air mobility: A comprehensive review and comparative analysis with autonomous and electric ground transportation for informing future research," *Transportation Research Part C: Emerging Technologies*, vol. 132, p. 103377, 2021.

(5) Y. Tsuji, D. Yashiro, Y. Kato, S. Bando, K. Yubai, and S. Komada, "Design of a thrust controller for propeller driven systems operating at multiple wind velocities and propeller angular velocities," *IEEJ Journal of Industry Applications*, vol. 12, no. 6, pp. 1060–1067, 2023.

(6) K. Yokota and H. Fujimoto, "Pitch angle control by regenerative air brake for electric aircraft," *IEEJ Journal of Industry Applications*, vol. 11, no. 2, pp. 308–316, 2022.

(7) K. Yokota and H. Fujimoto, "Aerodynamic force control for tilt-wing eVTOL using airflow vector estimation," *IEEE Transactions on Transportation Electrification*, vol. 8, no. 4, pp. 4163–4172, 2022.

(8) Y. Naoki, S. Nagai, and H. Fujimoto, "Mode-switching algorithm to improve variable-pitch-propeller thrust generation for drones under motor current limitation," *IEEE/ASME Transactions on Mechatronics*, vol. 28, no. 4, pp. 2003–2011, 2023.

(9) M. Sato and K. Muraoka, "Flight controller design and demonstration of quad-tilt-wing unmanned aerial vehicle," *Journal of Guidance, Control, and Dynamics*, vol. 38, no. 6, pp. 1071–1082, 2015.

(10) P. Hartmann, C. Meyer, and D. Moormann, "Unified velocity control and flight state transition of unmanned tilt-wing aircraft," *Journal of Guidance, Control, and Dynamics*, vol. 40, no. 6, pp. 1348–1359, 2017.

(11) D. Rohr, T. Stastny, S. Verling, and R. Siegwart, "Attitude and cruise control of a VTOL tiltwing UAV," *IEEE Robotics and Automation Letters*, vol. 4, no. 3, pp. 2683–2690, 2019.

(12) D. Rohr, M. Studiger, T. Stastny, N. R. J. Lawrance, and R. Siegwart, "Nonlinear model predictive velocity control of a VTOL tiltwing UAV," *IEEE Robotics and Automation Letters*, vol. 6, no. 3, pp. 5776–5783, 2021.

(13) E. Sariyildiz, H. Sekiguchi, T. Nozaki, B. Ugurlu, and K. Ohnishi, "A stability analysis for the acceleration-based robust position control of robot manipulators via disturbance observer," *IEEE/ASME Transactions on Mechatronics*, vol. 23, no. 5, pp. 2369–2378, 2018.

(14) W.-H. Chen, J. Yang, L. Guo, and S. Li, "Disturbance-observer-based control and related methods—an overview," *IEEE Transactions on industrial electronics*, vol. 63, no. 2, pp. 1083–1095, 2015.

(15) X. Lyu, J. Zhou, H. Gu, Z. Li, S. Shen, and F. Zhang, "Disturbance observer based hovering control of quadrotor tail-sitter VTOL UAVs using H_∞ synthesis," *IEEE Robotics and Automation Letters*, vol. 3, no. 4, pp. 2910–2917, 2018.

(16) Z. Chen, C. Liu, H. Su, X. Liang, and M. Zheng, "A hybrid disturbance observer for delivery drone's oscillation suppression," *Mechatronics*, vol. 88, p. 102907, 2022.

(17) B.-M. Nguyen, T. Kobayashi, K. Sekitani, M. Kawanishi, and T. Narikiyo, "Altitude control of quadcopters with absolute stability analysis," *IEEJ Journal of Industry Applications*, vol. 11, no. 4, pp. 562–572, 2022.

(18) APC prpeller, https://www.apcprop.com/technical-information/performance-data/, Accessed 9 Nov. 2023.

(19) R. E. Sheldahl and P. C. Klimas, "Aerodynamic characteristics of seven symmetrical airfoil sections through 180-degree angle of attack for use in aerodynamic analysis of vertical axis wind turbines," tech. rep., Sandia National Laboratories, 1981.

(20) T. Henderson, R. Favour, B. Hamlen, I. Mitha, E. Bowe, and N. Papanikolopoulos, "Hovering locomotion for UAVs with thrust-vectoring control surfaces," *IEEE Robotics and Automation Letters*, vol. 7, no. 2, p. 5214–5221, 2022.

Takuma Katagiri (Student Member) received the B.E. degree from the Department of Applied Physics and Physico-Informatics, Keio University, Yokohama, Japan in 2023. He is currently working towards his M.E. degree at the Department of Electrical Engineering and Information Systems, The University of Tokyo, Kashiwa, Japan. His research interests include motion control of electric flying mobility.

Kentaro Yokota (Non-member) received his M.S. degree from the University of Tokyo, Japan, in 2022. He is a researcher at the Research and Development Directorate, JAXA. He has been engaged in research and development of spacecraft guidance, navigation, and control systems. He is a Member of the Institute of Electrical and Electronics Engineers and the American Institute of Aeronautics and Astronautics.

Kota Fujimoto (Student Member) received the B.E. degree from the Department of Aeronautics and Astronautics, and the M.S. degree from the Department of Advanced Energy, The University of Tokyo, Kashiwa, Japan, in 2021 and 2023. He is currently working towards his Ph.D. degree at the Department of Electrical Engineering and Information Systems, The University of Tokyo. His research interests include UAV, motion control, wireless power transfer, and system design. He is a student member of the Institute of Electrical and Electronics Engineers, the American Institute of Aeronautics and Astronautics, and the Society of Automotive Engineers of Japan.

Sakahisa Nagai (Member) received the B.E., M.E., and Ph.D. degrees in electrical and computer engineering from the Department of Electrical and Computer Engineering, Yokohama National University, Kanagawa, Japan, in 2014, 2016, and 2019, respectively. Since 2019, he has been a project Assistant Professor with the Graduate School of Frontier Sciences, The University of Tokyo, Kashiwa, Japan. His research interests include sensorless actuation, motion control, wireless power transfer, and power electronics.

Hiroshi Fujimoto (Senior Member) received the Ph.D. degree in electrical engineering from the Department of Electrical Engineering, The University of Tokyo, Japan, in 2001. In 2001, he joined the Department of Electrical Engineering, Nagaoka University of Technology, Niigata, Japan, as a Research Associate. From 2002 to 2003, he was a Visiting Scholar with the School of Mechanical Engineering, Purdue University, West Lafayette, IN, USA. In 2004, he joined the Department of Electrical and Computer Engineering, Yokohama National University, Yokohama, Japan, as a Lecturer, and became an Associate Professor in 2005. He was an Associate Professor with The University of Tokyo from 2010 to 2020 and has been a Professor since 2021. His interests include control engineering, motion control, nanoscale servo systems, electric vehicle control, motor drive, visual servoing, and wireless power transfer. Dr. Fujimoto was a recipient of the Best Paper Award from the IEEE Transactions on Industrial Electronics in 2001 and 2013, Isao Takahashi Power Electronics Award in 2010, Best Author Prize of SICE in 2010, the Nagamori Grand Award in 2016, First Prize Paper Award for the IEEE Transactions on Power Electronics in 2016, and IEEJ Industry Applications Society Distinguished Transaction Paper Award in 2018 and 2023. He is a Fellow of IEEE and Senior Member of IEEJ. He is also a member of the Society of Instrument and Control Engineers, Robotics Society of Japan, and Society of Automotive Engineers of Japan. He has been a Senior Editor for the IEEE/ASME Transactions on Mechatronics since 2022 and an Associate Editor for the IEEE Industrial Electronics Magazine since 2006. He has been a Chairperson of the JSAE Technology Board since 2022 and was a past Chairperson of the IEEE/IES Technical Committee on Motion Control from 2012 to 2013 and the JSAE vehicle electrification committee from 2014 to 2020.